FURTHER EXAMINATION OF THE VIBRATORY LOADS REDUCTION RESULTS FROM THE NASA/ARMY/MIT ACTIVE TWIST ROTOR TEST

Matthew L. Wilbur
m.l.wilbur@larc.nasa.gov

William T. Yeager, Jr.
w.t.yeager@larc.nasa.gov

Martin K. Sekula
m.k.sekula@larc.nasa.gov

U. S. Army Vehicle Technology Directorate
NASA Langley Research Center
Hampton, VA 23681, USA

The vibration reduction capabilities of a model rotor system utilizing controlled, strain-induced blade twisting are examined. The model rotor blades, which utilize piezoelectric active fiber composite actuators, were tested in the NASA Langley Transonic Dynamics Tunnel using open-loop control to determine the effect of active-twist on rotor vibratory loads. The results of this testing have been encouraging, and have demonstrated that active-twist rotor designs offer the potential for significant load reductions in future helicopter rotor systems. Active twist control was found to use less than 1% of the power necessary to operate the rotor system and had a pronounced effect on both rotating- and fixed-system loads, offering reductions in individual harmonic loads of up to 100%. A review of the vibration reduction results obtained is presented, which includes a limited set of comparisons with results generated using the second-generation version of the Comprehensive Analytical Model of Rotorcraft Aerodynamics and Dynamics (CAMRAD II) rotorcraft comprehensive analysis.

Nomenclature

AFC	Active Fiber Composite
ARES	Aeroelastic Rotor Experimental System
ATR	Active Twist Rotor
F_x	fixed-system longitudinal shear, + aft, lb
F_y	fixed-system lateral shear, + right, lb
F_z	fixed-system vertical shear, + up, lb
M_x	fixed-system rolling moment, + left wing up, in-lb
M_y	fixed-system pitching moment, + nose up, in-lb
M_z	fixed-system yawing moment, + clockwise, in-lb
IBC	Individual Blade Control
IDE	interdigitated electrode
PFC	piezoelectric fiber composite
R	rotor radius, ft
TDT	Transonic Dynamics Tunnel
C_L	rotor lift coefficient
α_s	rotor shaft angle-of-attack, + nose up, deg
μ	advance ratio

Introduction

Rotorcraft vibration and noise reduction, as well as increasing rotor performance and maneuverability, continue to be a primary concern of the rotorcraft research community. One promising means of attaining such goals is to define an efficient way to achieve helicopter rotor individual blade control without the need for hydraulic power in the rotating system. Numerous electromechanical approaches exploiting active (smart) material actuation mechanisms have been investigated for this purpose (ref. 1). The most widely explored active material actuation methods have employed either piezoelectrically-actuated flaps placed at discrete locations along the blade (refs. 2-8), or piezoelectric material distributed along the blade and used to directly control deformations (usually twist) in the host blade structure (refs. 8-16). The examination of one such concept, strain-induced blade twisting, is the subject of the current study.

The primary design constraint in both the active blade flap and the active blade twist approaches is the need to obtain high piezoelectric actuation forces and displacements with a minimum of actuator weight. An additional concern with flap actuation mechanisms is that they must be designed to fit within the geometric confines of the blade structure. Direct control of blade twisting using embedded piezoelectric materials, although simple conceptually, has proven to be difficult to implement with conventional piezoelectric materials. Over the past several years, however, piezoelectric fiber composite (PFC) actuators have been shown to have the proper combination of conformability and performance characteristics necessary to develop a useful individual blade control system (refs. 8, 11-16). In addition, recent improvements in PFC strain-actuation capacity (ref. 17) indicate the potential for far greater blade twist actuation than has been achieved to date. Thus, the viability of this class of actuators for rotorcraft vibration control is just now emerging.

In 1997, a cooperative effort between the NASA Langley Research Center, the Army Research Laboratory, and the MIT Active Materials and Structures Laboratory was developed to perform initial feasibility and proof-of-concept studies of active twist rotor (ATR) technologies. The ultimate goals of the ATR program are to provide a wind-tunnel demonstration of an active twist rotor concept that uses piezoelectric fiber composite actuators, to investigate the potential benefits of such a system to reduce rotorcraft vibrations and noise, and, to a lesser extent, investigate potential improvements in rotor performance. This is being accomplished using a four-bladed, 110-inch diameter aeroelastically-scaled wind-tunnel model rotor designed for testing in the heavy gas, variable density test medium of the NASA Langley Transonic Dynamics Tunnel (TDT) (ref. 18). The TDT is a unique facility that permits full-scale rotor tip Mach numbers, Froude numbers, and Lock numbers to be matched simultaneously at model scale. In particular, the reduced speed of sound in the heavy gas test medium

allows full-scale tip Mach numbers to be matched at lower rotational speeds and drive motor power.

References 12 through 15 document the design, fabrication, and bench and hover testing of a single Active Twist Rotor prototype blade. Subsequently, a full set of ATR blades was fabricated and forward-flight testing conducted in the Langley Transonic Dynamics Tunnel to assess the impact of active blade twist on rotating- and fixed-system vibratory loads and acoustic noise generation. Initial vibration reduction results were presented in reference 16, with an overview of the noise reduction performance presented in reference 19. The impact of active-twist on rotor performance has not yet been evaluated experimentally.

The current paper will build upon the promising forward-flight results presented in reference 16, which concluded that reductions in 4P fixed-system loads of 60% to 95% were achieved with 1.1° to 1.4° of active blade twist. The capacity of blade twist actuation to reduce or eliminate rotating- and fixed-system vibratory loads is more fully explored with additional results and flight condition sensitivity studies. Additionally, an initial set of analytical comparisons and power consumption results is presented.

ATR Model Test System

Wind Tunnel

Forward-flight testing was conducted in the Langley Transonic Dynamics Tunnel (TDT), shown in figure 1, in a heavy gas test medium at a constant density of 0.0047 slugs/ft^3. The TDT is a continuous-flow pressure tunnel capable of speeds up to Mach 1.2 at stagnation pressures up to 1 atm. The TDT has a 16-ft square slotted test section with cropped corners and a cross-sectional area of 248 ft^2. Either air or R-134a, a heavy gas, may be used as the test medium. The TDT is particularly suited for rotorcraft aeroelastic testing primarily because of three advantages associated with the heavy gas. First, the high density of the test medium allows model rotor components to be heavier; thereby more easily meeting structural design requirements while maintaining dynamic scaling. Second, the low speed of sound in R-134a (approximately 550 ft/sec) permits much lower rotor rotational speeds to match full-scale hover tip Mach numbers and reduces the time-scales associated with active control concepts and dynamic response. Finally, the high-density environment increases the Reynolds number throughout the test envelope, which allows more accurate modeling of the full-scale aerodynamic environment of the rotor system.

Model Helicopter Rotor Testbed

The ATR blades were tested on the Aeroelastic Rotor Experimental System (ARES) model helicopter rotor testbed shown in figures 2 and 3. The ARES is powered by a 47-hp electric motor through a two-stage, belt-driven transmission system. Rotor control is achieved by a conventional hydraulically-actuated rise-and-fall swashplate using three independent actuators. Similarly, a single hydraulic actuator controls rotor-shaft angle of attack.

Instrumentation on the ARES testbed permits continuous display of model control settings, rotor speed, rotor forces and moments, fixed-system accelerations, blade loads and position, and pitch-link loads. All rotating-system data are transferred through a 30-channel slip ring assembly to the testbed fixed system. An additional slip ring permits the transfer of high-voltage power from the fixed system to the rotating system for actuation of the AFC actuators embedded in the ATR blades. A six-component strain-gage balance placed in the fixed system 21.0 inches below the rotor hub measures rotor forces and moments. The strain-gage balance supports the rotor pylon and drive system, pitches with the model shaft, and measures all of the fixed-system forces and moments generated by the rotor model. A streamlined fuselage shape encloses the rotor controls and drive system; however, the fuselage shape is isolated from the rotor system such that its forces and moments do not contribute to the loads measured by the balance.

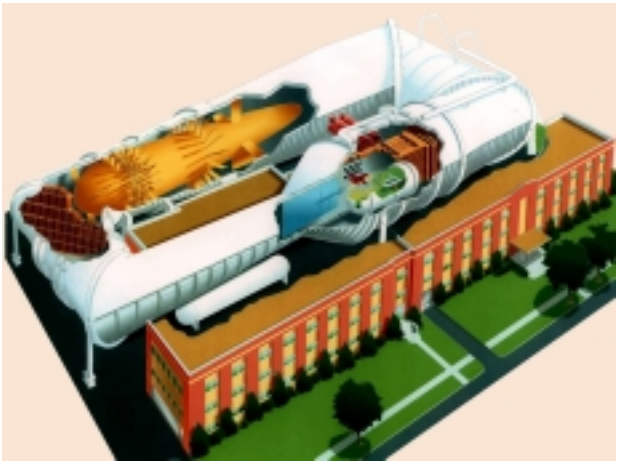

Figure 1. The Langley Transonic Dynamics Tunnel (TDT).

ATR Blades

Each Active Twist Rotor blade utilizes 24 commercially-available Active Fiber Composite (AFC) actuators to achieve active twist control. The AFC actuators, shown conceptually in figure 4, are embedded directly in the structure of each blade D-spar, spanning a section of uniform blade structure from 0.30R (30% blade radius) to 0.98R. The AFCs are placed in four layers through the blade thickness and are oriented such that the active strain is applied at

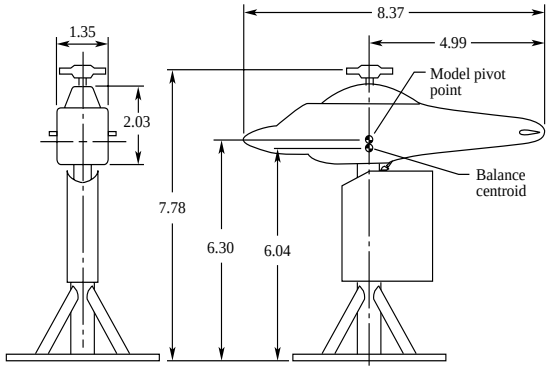

Figure 2. Schematic of the Aeroelastic Rotor Experimental System (ARES) helicopter testbed. All dimensions are in feet.

Figure 3. The ARES testbed in the TDT with the ATR hardware installed.

±45° relative to the blade spanwise axis to generate maximum torsional control of the blades. Four dedicated high-voltage amplifiers, one for each blade, are used to generate high voltage, low current power for the independent actuation of each blade.

The ATR blades, general parameters for which are provided in Table 1, have a rectangular planform with a chord of 4.24 inches, radius of 55.0 inches, a NACA-0012 airfoil, and a linear pretwist of -10° from the center of rotation to the blade tip. Testing was conducted at a constant rotor speed of 688 rpm (M_{tip} = 0.60) on a four-bladed articulated hub with coincident flap and lag hinges and trailing pitch links. Instrumentation on the ATR blades includes ten 4-arm strain-gage bridges, with results from the three most inboard strain gage bridges (flapwise, chordwise, and torsion) presented in the results section of this paper. ATR blade frequencies, determined by a combination of analysis and experimental observation, are presented in Table 2.

Computer Control System

Active-twist control of the ATR blades is achieved with a computer control system incorporating a digitalsignal processor, 32 analog-to-digital channels, 6 digital-to-analog channels, and 32 digital input-output channels. The control system may be used in an open-

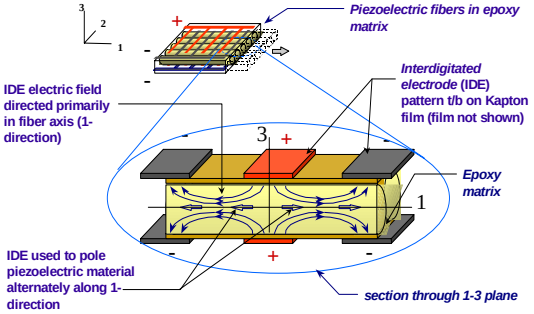

Figure 4. Active Fiber Composite (AFC) piezoelectric actuator concept.

Table 1. Active Twist Rotor General Parameters

Property	Description	Value
R	Blade radius, ft	4.583
c	Blade chord, ft	0.353
r_c	Root cutout, ft	1.04
θ_{pt}	Blade linear pretwist, deg	-10.0
N	Number of blades	4
e	Flap-lag hinge location, ft	0.25
Ω_0	Nominal rotor rotational speed, rpm	688
ρ_0	Nominal test medium density, slugs/ft^3	0.0047
M_{tip}	Blade hover tip Mach number	0.60
T_{1g}	Rotor thrust for simulated 1g flight, lb	225.0

Table 2. ATR Rotating Blade Frequencies

Mode	Frequency
Rigid Lag	0.29P
Rigid flap	1.04P
1st elastic flap	2.79P
2nd elastic flap	5.36P
1st elastic lag	6.07P
Elastic torsion	7.59P

loop fashion with the user prescribing either: 1) the amplitude and frequency of collective twist mode actuation, or 2) the amplitude, control phase, and harmonic frequency of actuation. For the first type of actuation, each blade is sent twist commands according to the equation:

$$V_{act} = A_{act} \cos \omega t$$

where V_{act} is the actuation voltage determined by the actuation voltage amplitude, A_{act}; the actuation frequency, ω_{act}; and time, t. This type of actuation is useful for sine dwell excitation for the development of system frequency response functions. With the second type of actuation, the active-twist commands are synchronized to the rotation of the rotor system such that proper actuation frequency and control phase are achieved, regardless of rotor speed. For this type of control, either "collective" twist mode or "individual blade control (IBC)" twist mode actuation may be selected. With the collective twist mode of actuation, each blade is sent twist commands simultaneously according to a schedule prescribed by the azimuthal position of a reference blade:

$$V_{Coll} = A_n \cos\left(n\psi_{ref} - \phi_n\right)$$

where V_{Coll} is the actuation voltage determined by the harmonic amplitude, A_n; the control harmonic, n; the control phase, ϕ_n; and the azimuthal position of the

reference blade, ψ_{ref}. For the IBC mode of actuation, each blade is sent twist commands according to a prescribed schedule associated with its own position in the rotor azimuth:

$$V_{IBC_b} = A_n \cos\left(n\psi_{ref} - 90^\circ(b-1) - \phi_n\right)$$

where V_{IBC_b} is the actuation voltage for the *b*th blade determined by the harmonic amplitude, A_n; the control harmonic, n; the control phase, φ_n; and the azimuthal position of the reference blade, ψ_{ref} (which is assumed to be blade 1 with blades 2, 3, and 4 trailing at 90° intervals).

Results

All testing was conducted in the heavy gas test medium of the TDT at a nominal density of 0.0047 slugs/ft³. The rotor rotational speed throughout the test was held at a constant 688 rpm resulting in a nominal hover tip Mach number, M_{tip}, of 0.60. The test matrix, presented in Table 3 in terms of advance ratio, μ, and rotor-shaft angle-of-attack, α_s, incorporated various steady-state trim conditions representative of sustained 1g level flight and descending flight at advance ratios ranging from 0.140 to 0.367. At each flight condition the rotor was trimmed to a nominal rotor lift coefficient, C_L, of 0.0066 and the first-harmonic blade flapping with respect to the shaft was trimmed to within 0.1°.

For each condition tested, data were acquired with active twist control disabled. These sets of data are referred to throughout the paper as the "baseline" conditions. Typically, several sets of baseline data were acquired to establish a set of well-determined baseline loads and conditions. The effect of active twist control was then tested by selecting the type of actuation: collective or IBC twist; the actuation voltage amplitude, typically 500 V, 750 V, or 1000 V; and the harmonic frequency of actuation, typically 3P, 4P, or 5P. The ATR computer control system was used to automatically actuate the rotor system with the prescribed amplitude, control type, and frequency parameters at a sequence of control phases beginning with 0° and progressing to 360° in 20° increments. At each control phase increment the control conditions were held, permitting the rotor and fixed-system transient responses to dampen, then data were acquired automatically on the data acquisition computer systems. Measurements were made for 19 control phases with the first measurement made at a control phase of 0° and the final measurement in the sequence (360°) being a repeat of the first.

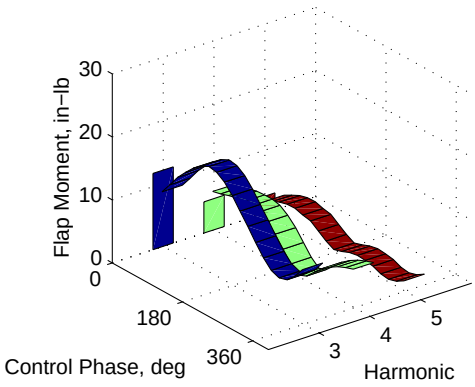

Figure 5. Sample ribbon plot. Blade flapwise bending moment (0.29R) for 3P IBC control. μ = 0.140, C_L = 0.0066, α_s = -1.0°, and 1000 V actuation amplitude.

Figure 5 presents the typical method used to convey ATR rotating-system response in reference 16. The figure presents a "ribbon plot" of the blade flapwise bending moment measured at 0.29R for 3P IBC active twist control at μ = 0.140, C_L = 0.0066, α_s = -1.0°, and 1000 V actuation voltage amplitude. Each of the "ribbons" represents the changing 3P, 4P, and 5P harmonic blade responses as a function of active twist control phase. The vertical bars on the rear surface of the plots (at 0° control phase) are representative of the harmonic loads generated by the baseline (control off)

Table 3. ATR Forward Flight Test Matrix

	μ = 0.140	μ = 0.170	μ = 0.200	μ = 0.233	μ = 0.267	μ = 0.300	μ = 0.333	μ = 0.367
α_s = +8º	X							
α_s = +5º	X							
α_s = +4º	X	X	X	X	X			
α_s = +2º	X			X	X			
α_s = +1º		X						
α_s = 0º	X		X	X	X			
α_s = -1º	X	X	X					
α_s = -2º	X			X	X			
α_s = -4º						X	X	
α_s = -6º							X	X
α_s = -8º							X	

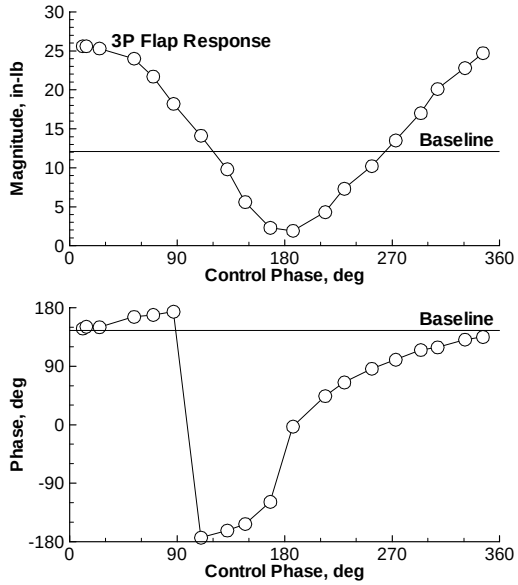

Figure 6. Sample response plot. Blade flapwise bending moment (0.29R) for 3P IBC control. μ = 0.140, C_L = 0.0066, α_s = -1.0°, and 1000 V actuation.

condition. Another means for viewing the data set is presented in figure 6, in which only the 3P response is presented for clarity. The upper plot in figure 6 presents the magnitude of the response as a function of active twist control phase. The solid horizontal line spanning the plot represents the baseline response. The lower figure presents the response phase as a function of the control phase, with the horizontal line indicating the baseline phase. The results as presented in figures 5 and 6 are useful for providing an overview of the effect that active blade twist has on system loads. However, important details are unavailable with the plot formats of figures 5 and 6 that are critical to a thorough understanding of the vibration reduction potential of the active-twist concept. For example, figure 7 presents the 3P response results from figures 5 and 6 in another, generally more informative, format.

Figure 7 presents the rotating-system 3P response in a response map or "circle plot" format for the baseline (no control) condition, and 3P active twist actuation voltages of 500 V, 750 V, and 1000 V. The plots present the 3P sine component of the response as a function of the 3P cosine component of the response, so that both response magnitude and response phase are evident in the results. The solid circle represents the baseline condition, while the three open symbols represent the response measured during twist actuation. A radial line is presented on the plot to reference the location of the response due to 0° control phase. Control phase angles advance around the plots counterclockwise. The advantage of this plot type is that it directly shows the relationship between the baseline response, the response for varying actuation voltage amplitudes, and the zero harmonic load condition represented by the origin of each plot. A plot in which the "circle" of response points encompasses the origin represents a condition for which sufficient control authority exists to eliminate that particular harmonic load. As shown in figure 7, 3P harmonic loads for the blade flapwise bending moment may be "zeroed" for the condition presented (μ = 0.140, C_L = 0.0066, α_s = -1.0°, 3P IBC actuation). Thus, significantly more

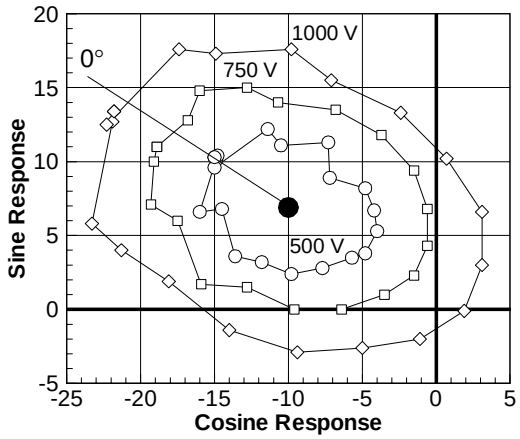

Figure 7. Sample response map or "circle plot." Blade flapwise bending moment (0.29R) for 3P IBC control. μ = 0.140, C_L = 0.0066, α_s = -1.0°, and 1000 V actuation.

information is conveyed by the "circle plot" format when compared to the "ribbon plot" format, thereby permitting a more thorough evaluation of the test results.

Low-Speed Flight

Generally, the highest baseline fixed-system loads were observed for the transition flight speed, μ = 0.140. It was also observed that the highest fixed-system loads were predominately at the more negative (shaft forward) angles of attack, and that the IBC blade control was the most effective in minimizing the majority of the system loads throughout the flight conditions tested. This paper, therefore, shall concentrate on the test results acquired at μ = 0.140, C_L = 0.0066, and α_s = -1.0°, as this is considered to be the "worst case" condition. Likewise, the results presented will be those acquired with the IBC active twist control to provide an indication of the maximum vibration reduction control authority achieved.

Figures 8, 9, and 10 present results in the circle plot format for 3P, 4P, and 5P active twist actuation, respectively, at the maximum, 1000 V, IBC actuation amplitude. Results presented in each figure include the blade flapwise (a) and chordwise (b) response at 0.29R, the blade torsional (c) response at 0.34R, the pitch link (d) response, and the six fixed-system balance (e through j) responses. Rotating-system (flap, chord, torsion, and pitch link) plots include 3P, 4P, and 5P response results represented by circles, squares, and diamonds, respectively. Fixed-system results present only 4P responses. For each plot, solid symbols indicate the baseline, no control, response. Where possible, radial lines are shown to indicate the 0° control phase response.

Examination of figures 8 through 10 shows that significant blade torsional loads (subplot c) are generated at the frequency of twist actuation. Pitch link loads (subplot d), while remaining small for 3P twist actuation, increase greatly at the actuation frequency for 4P and 5P actuation, and are always higher in response magnitude than the corresponding baseline case. Blade flapwise bending loads (subplot a) are shown to be most sensitive to actuation at 3P and 5P due to the proximity of the first and second blade flapwise elastic frequencies. A similar phenomenon is also identifiable in the blade chordwise bending loads

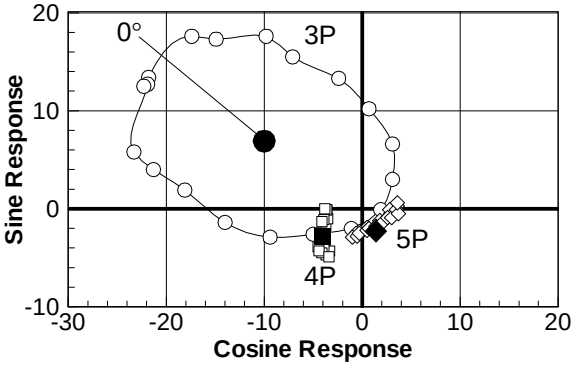

(a) Blade flapwise moment (r/R = 0.29), in-lb

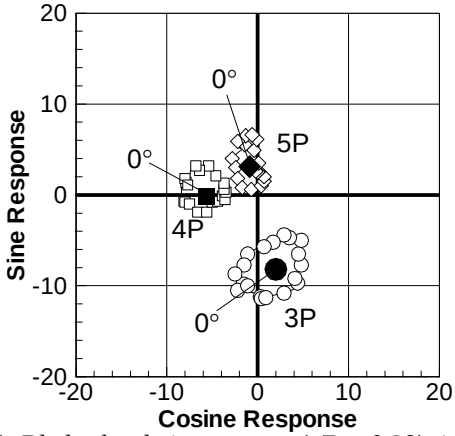

(b) Blade chordwise moment (r/R = 0.29), in-lb

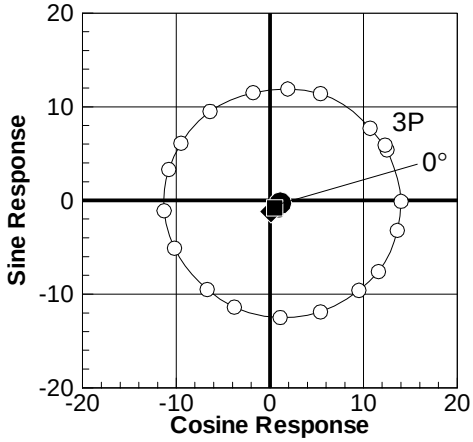

(c) Blade torsion moment (r/R = 0.34), in-lb

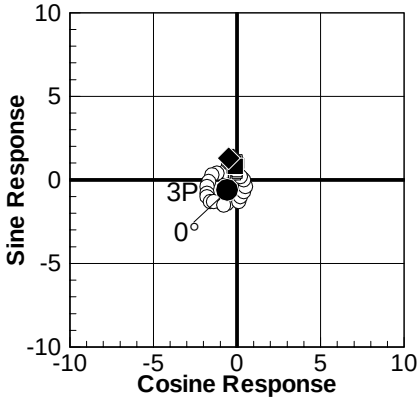

(d) Pitch link load, lb

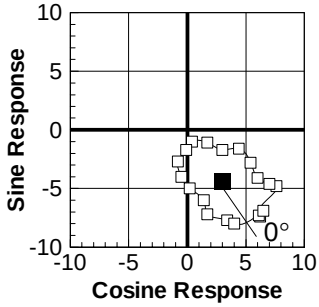

(e) 4P longitudinal shear (F_x), lb

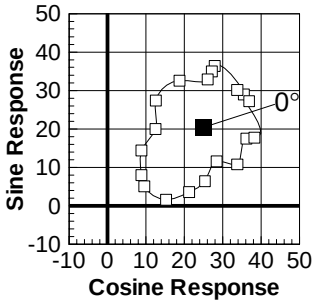

(f) 4P lateral shear (F_y), lb

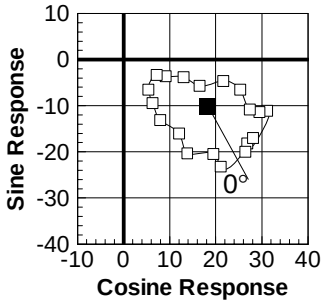

(g) 4P vertical shear (F_z), lb

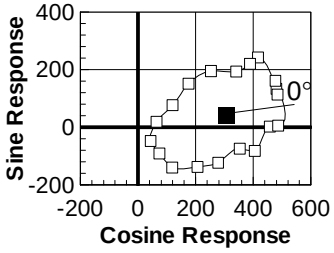

(h) 4P rolling moment (M_x), in-lb

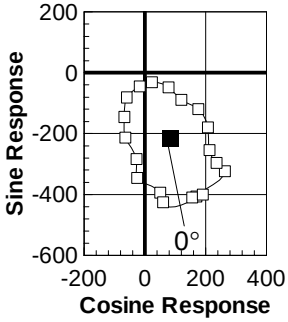

(i) 4P pitching moment (M_y), in-lb

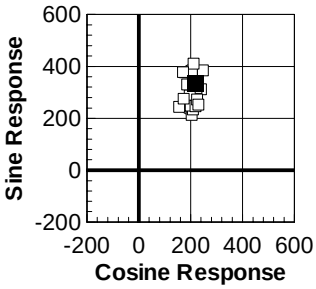

(j) 4P yawing moment (M_z), in-lb

Figure 8. Rotating- and fixed-system response maps for μ = 0.140, C_L = 0.0066, α_s = -1.0°, and 3P, 1000 V IBC actuation.

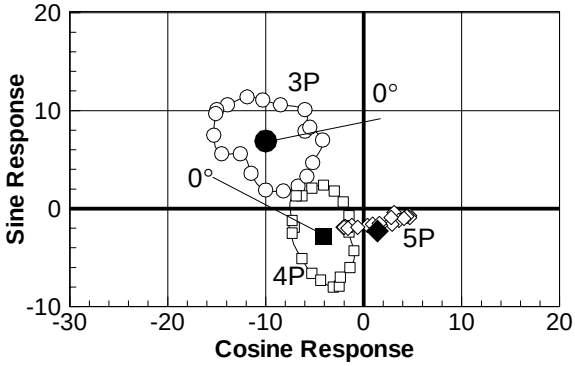

(a) Blade flapwise moment (r/R = 0.29), in-lb

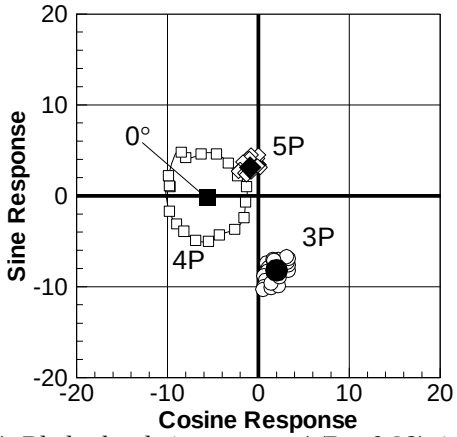

(b) Blade chordwise moment (r/R = 0.29), in-lb

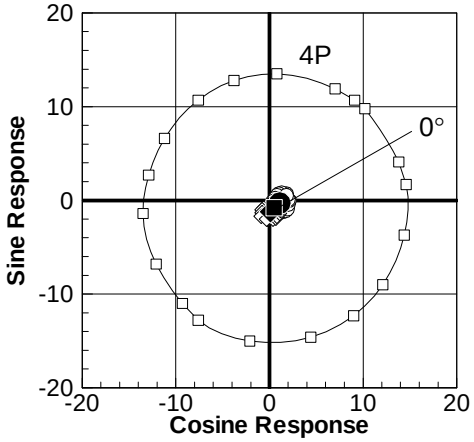

(c) Blade torsion moment (r/R = 0.34), in-lb

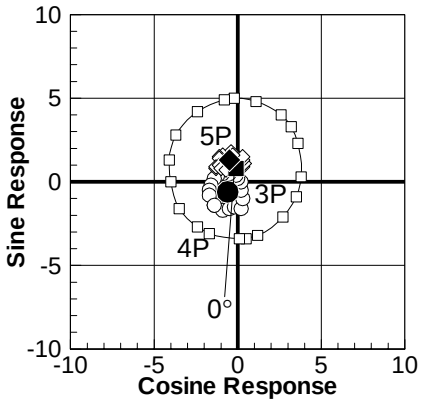

(d) Pitch link load, lb

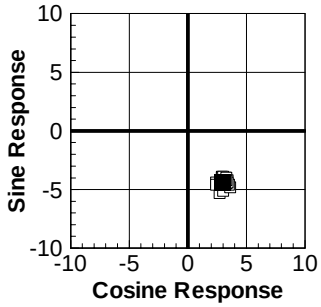

(e) 4P longitudinal shear (F_x), lb

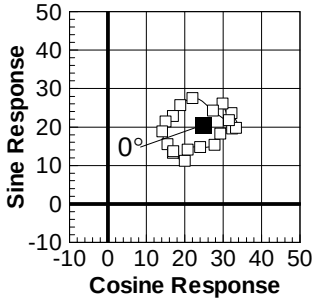

(f) 4P lateral shear (F_y), lb

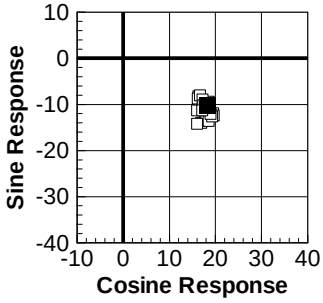

(g) 4P vertical shear (F_z), lb

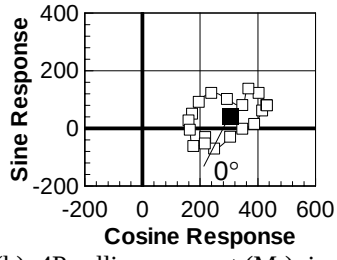

(h) 4P rolling moment (M_x), in-lb

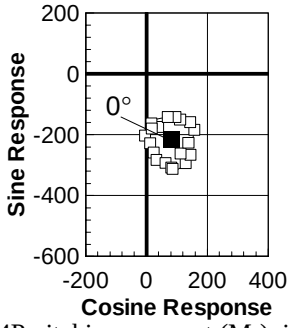

(i) 4P pitching moment (M_y), in-lb

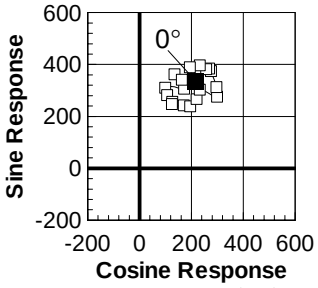

(j) 4P yawing moment (M_z), in-lb

Figure 9. Rotating- and fixed-system response maps for μ = 0.140, C_L = 0.0066, α_s = -1.0°, and 4P, 1000 V IBC actuation.

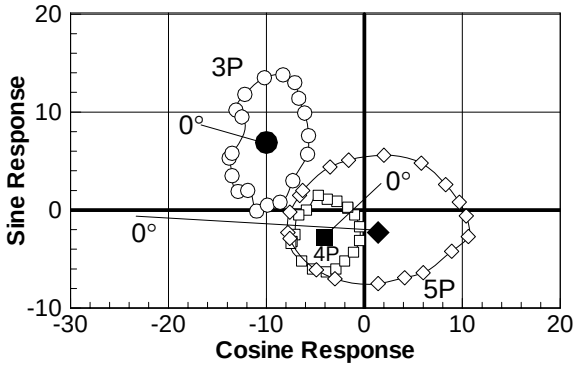

(a) Blade flapwise moment (r/R = 0.29), in-lb

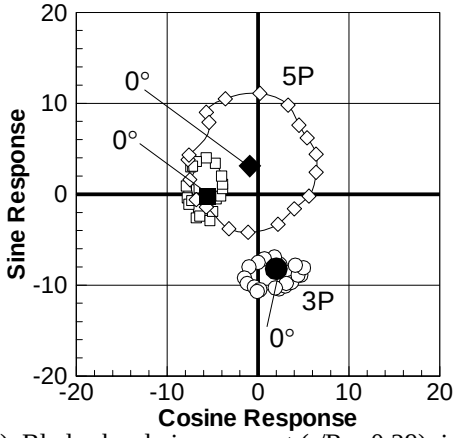

(b) Blade chordwise moment (r/R = 0.29), in-lb

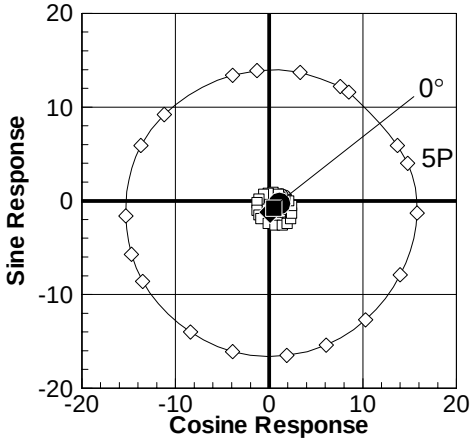

(c) Blade torsion moment (r/R = 0.34), in-lb

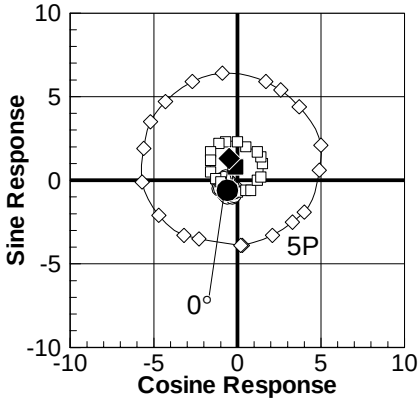

(d) Pitch link load, lb

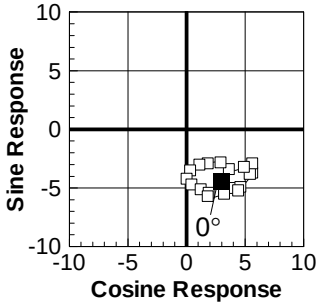

(e) 4P longitudinal shear (F_x), lb

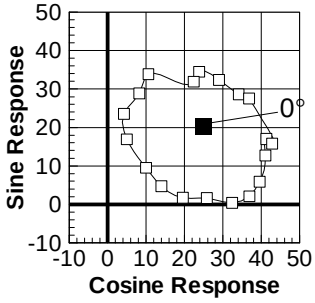

(f) 4P lateral shear (F_y), lb

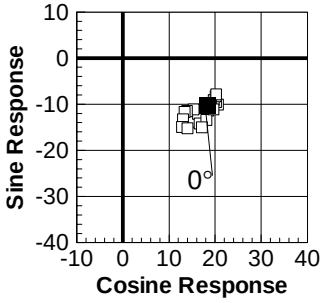

(g) 4P vertical shear (F_z), lb

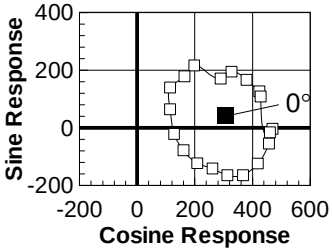

(h) 4P rolling moment (M_x), in-lb

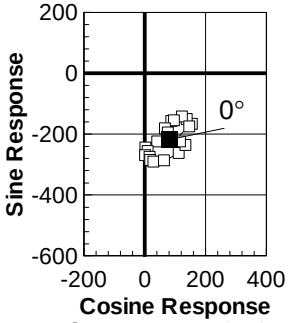

(i) 4P pitching moment (M_y), in-lb

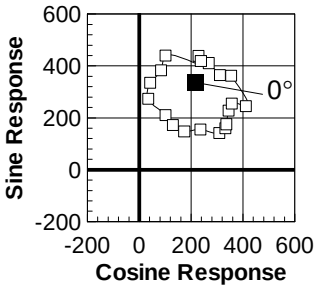

(j) 4P yawing moment (M_z), in-lb

Figure 10. Rotating- and fixed-system response maps for μ = 0.140, C_L = 0.0066, α_s = -1.0°, and 5P, 1000 V IBC actuation.

(subplot b) that are shown to be increasingly sensitive to the higher actuation harmonics. The 3P blade twist actuation (figure 8) provides generally the greatest control authority over the fixed-system vibratory loads, where reductions of 70% to 95% are evident for all fixed-system loads except for yawing moment, which is generally unresponsive to 3P actuation. Further, fixed-system vibratory loads are very nearly minimized simultaneously when the blades are actuated at 3P for control phases between 180° and 200°. Figure 9 shows that the 4P blade actuation provides the least control authority over the fixed-system loads, even for the vertical load where the 4P actuation was expected to provide the greatest load reductions. Figure 10 presents the results for 5P blade actuation, which is effective in providing control of fixed-system lateral forces and yawing and rolling moments although does not offer the depth of load reductions evident in the 3P actuation results (presented in figure 8). It is noted that the 5P actuation appears to over-excite the 5P blade flapwise and chordwise bending responses so that lower 5P actuation voltage amplitudes (less than 300 V) may offer greater fixed-system load reductions. Although these observations specifically address the results presented in figures 8 through 10, similar trends were observed at other advance ratios. In general, 3P IBC actuation was shown to provide the greatest potential for vibration reduction across the flight speed range tested, although control phase and actuation voltage for component load minimization was shown to vary more than is evident in figures 8 through 10.

Effect of the Rotating-System on Fixed-System Loads. Of specific concern in evaluating the results presented in figures 8 through 10 is the effect that loads changing in the rotating-system have on those in the fixed-system. As has been well-documented throughout the literature, a rotor system with a matched set of N equally-spaced blades will act as a filter such that only the harmonic loads that are multiples of the number of blades are transferred to the fixed-system. Thus, for a 4-bladed rotor system such as the ATR, one may expect to observe in the higher-harmonic fixed-system: 4P loads, 8P loads, 12P loads, etc. These loads are generated in the rotating-system by harmonic loads at nN and nN±1, where n = 1, 2, 3, … Academically speaking, one would expect that 4P rotating-system loads will most greatly impact the 4P fixed-system vertical shear (F_z), and the 4P fixed-system yawing moment (M_z). Likewise, the remaining fixed-system loads -- the 4P longitudinal (F_x) and lateral (F_y) shears, and the 4P pitching (M_y) and rolling (M_x) moments -- should be most affected by the 3P and 5P rotating-system loads. It is useful, therefore, to identify evidence of such phenomena within the results.

One example of the effect of rotating-system loads on the fixed-system is presented in figure 11. In this figure, the 3P blade flapwise bending moment, the 3P pitch link load, and the associated 4P fixed-system rolling and pitching moment responses due to 3P blade actuation at 1000 V are presented for a flight condition of μ = 0.140, C_L = 0.0066, and α_s = -1.0°. For this condition, the 3P blade chordwise moment and the 5P rotating-system loads were found to contribute little to the overall 4P fixed-system response. As presented, the 3P blade flapwise moment (figure 11a) reaches a minimum load along the 180° control phase radial line.

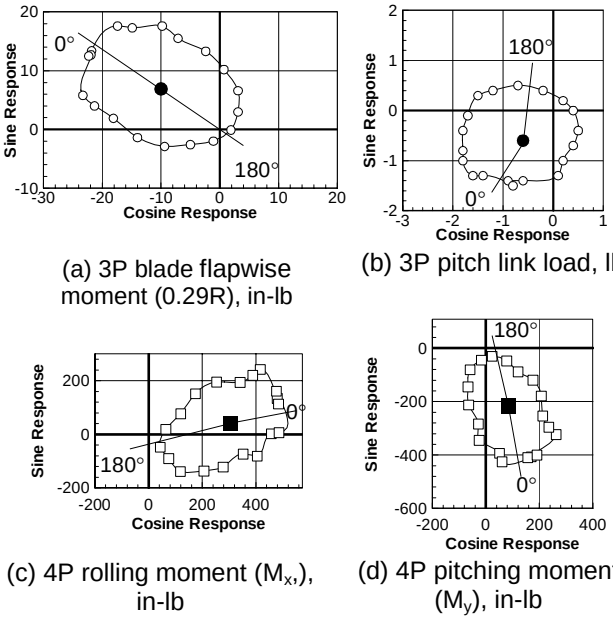

(a) 3P blade flapwise moment (0.29R), in-lb

(b) 3P pitch link load, lb

(c) 4P rolling moment (M_x,), in-lb

(d) 4P pitching moment (M_y), in-lb

Figure 11. Rotating- to fixed-system loads comparison for μ = 0.140, C_L = 0.0066, α_s = -1.0°, and 3P, 1000 V IBC actuation.

At this condition, the 3P pitch link load (figure 11b), which is already relatively small, is also nearly minimized. The associated effect in the fixed-system is presented for the 4P rolling and pitching moments (figures 11c and 11d, respectively), which shows that each of these loads are very nearly minimized along the 180°, as well. Similar trends may be observed in the experimental results for other flight conditions, actuation frequencies, and rotating- and fixed-system load combinations.

Vibration Sensitivity Studies

Clearly, a vibration reduction method is impractical if its application is limited to a small region of the flight envelope; therefore, the variation in vibratory loads with changing flight conditions is of considerable interest. Testing conducted to date on the ATR has not included thrust variation, however, a range of shaft angles-of-attack and advance ratios has been assessed. Each of these will be examined in the following sections.

Shaft Angle-of-Attack Sensitivity. Figures 12 through 15 present the circle plots for three 4P fixed-system loads (F_x, F_z, and M_y) at four different shaft angles-of-attack (α_s = +8.0°, +5.0°, +2.0°, and -1.0°) for μ = 0.140, C_L = 0.0066, and 3P IBC actuation at 1000 V amplitude. As presented in figures 12 through 15, the shapes of the control authority regions remain relatively circular until the rotor-shaft tilt (α_s) becomes negative. It is also evident that the total area of the individual control authority regions remains approximately the same as the rotor shaft angle-of-attack changes. Therefore, it is the location of the baseline condition in the response map that determines whether a particular response can be eliminated at a given flight speed. It is also noted that a zero condition may be achieved for all of the positive shaft angle-of-attack (rearward shaft tilt) conditions, therefore, active twist control appears to be applicable for the reduction of descent condition vibratory loads.

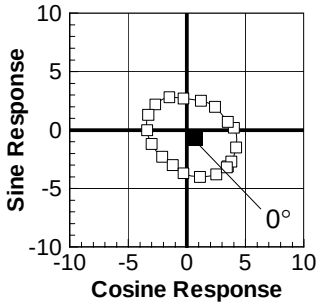

(a) 4P longitudinal shear (F_x), lb

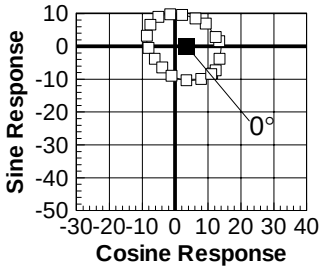

(b) 4P vertical shear (F_z), lb

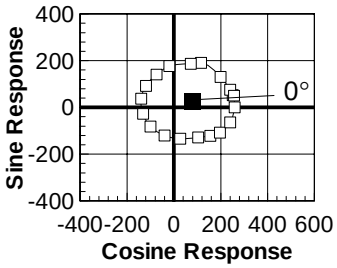

(c) 4P rolling moment (M_x), in-lb

Figure 12. Response maps for μ = 0.140, C_L = 0.0066, α_s = +8.0°, and 3P, 1000 V IBC actuation.

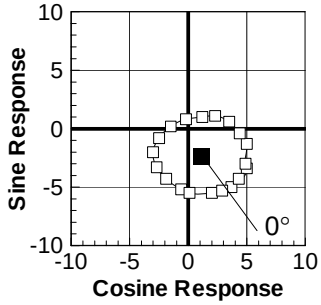

(a) 4P longitudinal shear (F_x), lb

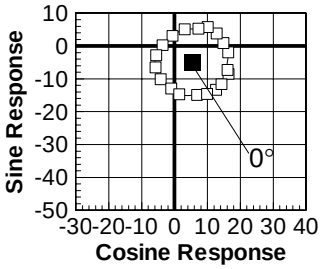

(b) 4P vertical shear (F_z), lb

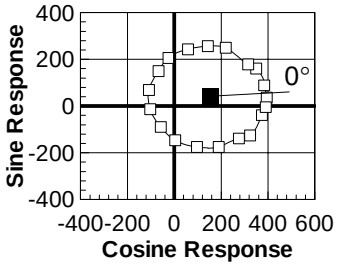

(c) 4P rolling moment (M_x), in-lb

Figure 13. Response maps for μ = 0.140, C_L = 0.0066, α_s = +5.0°, and 3P, 1000 V IBC actuation.

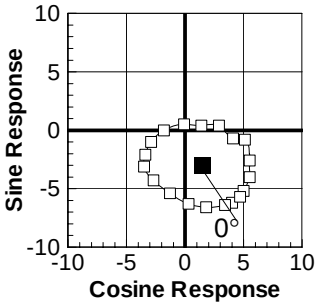

(a) 4P longitudinal shear (F_x), lb

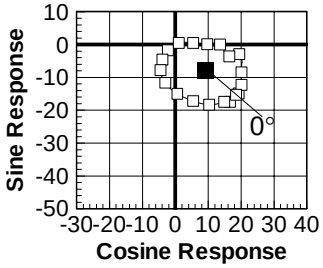

(b) 4P vertical shear (F_z), lb

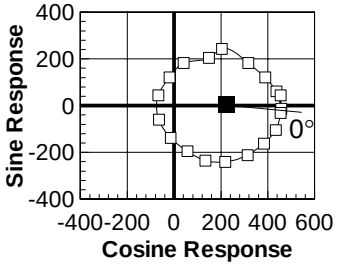

(c) 4P rolling moment (M_x), in-lb

Figure 14. Response maps for μ = 0.140, C_L = 0.0066, α_s = +2.0°, and 3P, 1000 V IBC actuation.

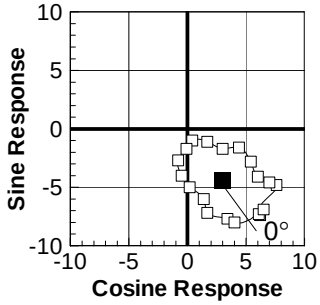

(a) 4P longitudinal shear (F_x), lb

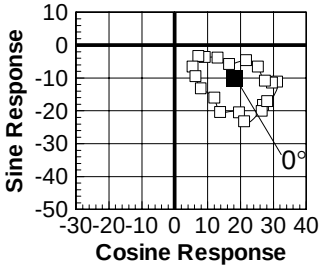

(b) 4P vertical shear (F_z), lb

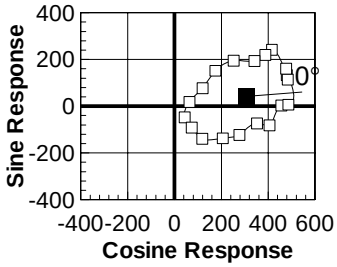

(c) 4P rolling moment (M_x), in-lb

Figure 15. Response maps for μ = 0.140, C_L = 0.0066, α_s = -1.0°, and 3P, 1000 V IBC actuation.

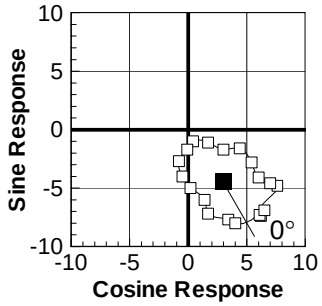

(a) 4P longitudinal shear (F_x), lb

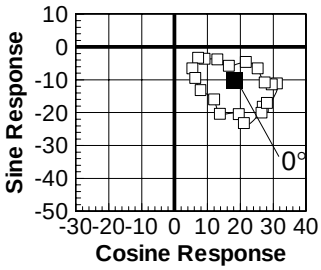

(b) 4P vertical shear (F_z), lb

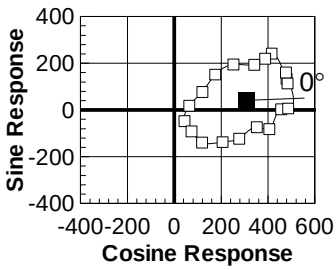

(c) 4P rolling moment (M_x), in-lb

Figure 16. Response maps for μ = 0.140, C_L = 0.0066, α_s = -1.0°, and 3P, 1000 V IBC actuation.

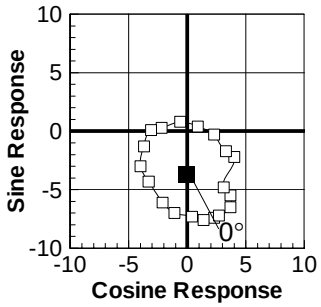

(a) 4P longitudinal shear (F_x), lb

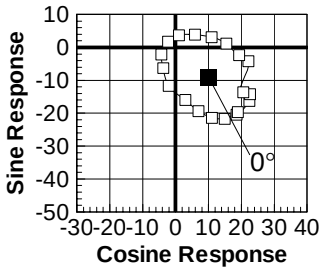

(b) 4P vertical shear (F_z), lb

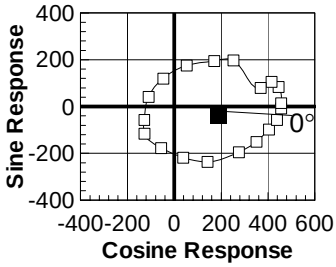

(c) 4P rolling moment (M_x), in-lb

Figure 17. Response maps for μ = 0.200, C_L = 0.0066, α_s = -1.0°, and 3P, 1000 V IBC actuation.

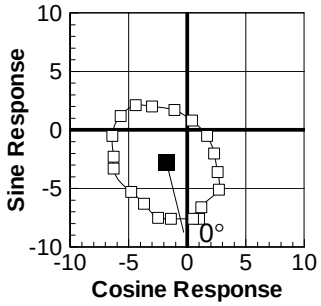

(a) 4P longitudinal shear (F_x), lb

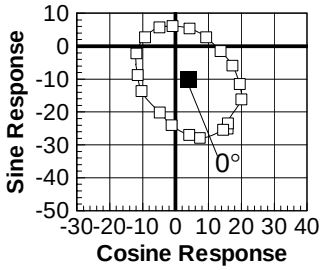

(b) 4P vertical shear (F_z), lb

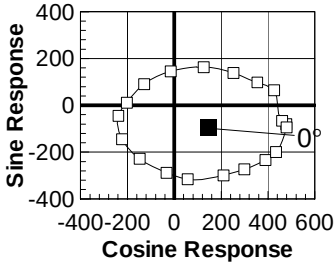

(c) 4P rolling moment (M_x), in-lb

Figure 18. Response maps for μ = 0.267, C_L = 0.0066, α_s = -2.0°, and 3P, 1000 V IBC actuation.

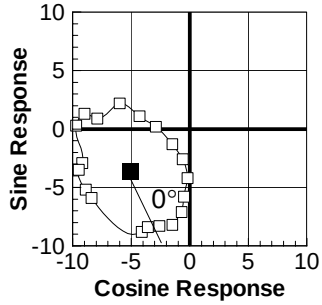

(a) 4P longitudinal shear (F_x), lb

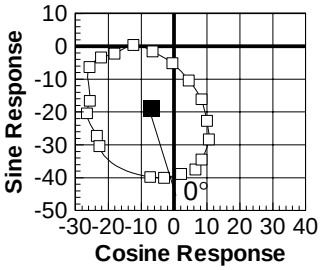

(b) 4P vertical shear (F_z), lb

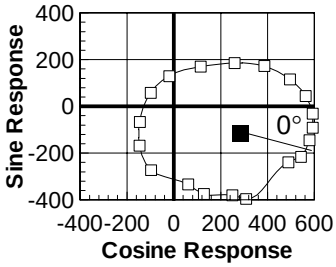

(c) 4P rolling moment (M_x), in-lb

Figure 19. Response maps for μ = 0.333, C_L = 0.0066, α_s = -6.0°, and 3P, 1000 V IBC actuation.

Flight Speed Sensitivity. Figures 16 through 19 present the circle plots for the three 4P fixed-system loads (F_x, F_z, and M_y) at four different flight speeds (μ = 0.140, 0.200, 0.267, and 0.333) for C_L = 0.0066 and 3P IBC actuation at 1000 V amplitude. The shaft angle-of-attack was varied through the speed range to simulate a 1g sustained flight condition. As presented in figures 16 through 19, a substantial increase in the size of the control authority regions is evident as the flight speed increases. Some change is evident in the shape of the control authority regions, however, no more than that noted for the shaft angle-of-attack sensitivity. A zero condition is within the twist control limits for each of the fixed-system loads through the middle flight speed ranges (μ = 0.200 and μ = 0.267), with a zero condition for rolling moment extending up to μ = 0.333. By inspecting figure 16c, it may be concluded that a voltage amplitude of approximately 500 V at an active twist control phase of 150° is sufficient to eliminate the rolling moment at μ = 0.267. To eliminate the vertical shear (figure 16a) would require a voltage amplitude of approximately 700 V at a control phase of 180°. This illustrates the need to apply a closed-loop control scheme that can effectively optimize the active-twist actuation commands to yield a minimized vibration index. This vibration index would be generated by combining the weighted responses of multiple fixed-system loads to suit the particular requirements of the encountered flight condition, and could be tailored to a variety of vibration reduction goals.

Overall Vibration Reduction Capacity

Figures 8 through 19 present a sampling of the results obtained during the initial forward flight test of the NASA/Army/MIT Active Twist Rotor in the TDT. As presented, significant vibration reduction or vibration elimination has been demonstrated for all 4P fixed-system balance loads, with the exception of yawing moment, throughout the flight speed range. In general, actuation schedules using 3P IBC active blade twist were found to be the most effective in minimizing 4P fixed-system loads. Of the 26 different forward-flight conditions tested, all but three offer combinations of actuation harmonic, voltage amplitude, and control phase that will eliminate at least three components of the 4P fixed-system loads, although not necessarily simultaneously.

Active Twist Power

Of significant concern during the development of an active vibration suppression system is the amount of power necessary for effective vibration reduction. The RMS electrical power required to actuate the ATR blades was determined to be primarily a linear function of actuation frequency, as presented in figure 20. Minor variations in power required to actuate the blades were noted with changes in rotor shaft pitch and forward flight speed, however, these variations were clearly secondary to the power required due to actuation frequency. The amount of power required to operate all four blades simultaneously is presented in figure 20 as a function of actuation frequency. The total power absorbed by the blades for 5P actuation (73 Watts RMS) has been found to represent less than 0.9% of the maximum rotor power necessary for the flight conditions tested.

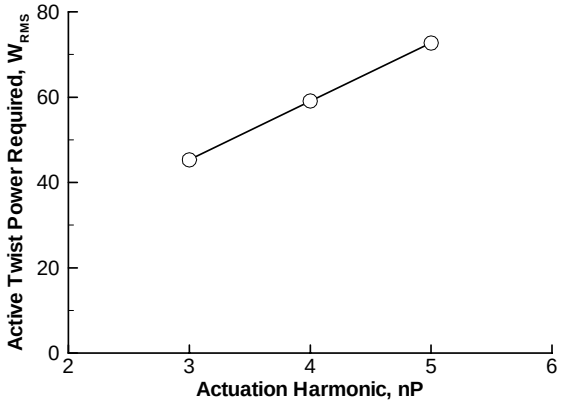

Figure 20. Rotor actuation power required.

Analysis Comparison

The practical development of active blade twist technology for vibration reduction hinges largely on the capacity of analytical methods to capture the response characteristics of such rotor systems. Throughout the development of the NASA/Army/MIT Active Twist Rotor design, the second-generation version of the Comprehensive Analytical Model of Rotorcraft Aerodynamics and Dynamics (CAMRAD II) (ref. 20) was used extensively for blade frequency response, blade load, and fixed-system load reduction calculations. As discussed in references 12 and 15, CAMRAD II has no direct facility for modeling the strain-induced actuation of a rotor blade with embedded Active Fiber Composite actuators. Instead, an external torsional couple is applied to the blade near the root and at the tip to simulate the internal torsional moments developed by the AFCs. Input parameters permit the selection of active twist harmonic actuationfrequency, amplitude, and phase.

Although extensive comparisons between a CAMRAD II model and the test results have not yet been completed, an initial set of comparisons are presented in figures 21 through 23 for an isolated-rotor model developed in CAMRAD II. For these results, the CAMRAD II model was initially run to establish the rotor loads and control positions for the baseline, no twist actuation, case. Then the blade torsional actuation moment for each actuation frequency was selected by adjusting its amplitude until the change in tip twist between the baseline case and the 0° control phase angle case matched measured values for the three actuation frequencies. Holding the control positions and twist actuation moment fixed, the analytical model was exercised for 3P, 4P, and 5P twist actuations using control phase angles from 0° to 315° in 45° increments.

The results of the analysis for each actuation frequency are presented with the corresponding wind tunnel test results in figures 21 through 23 for a flight condition of μ = 0.140, C_L = 0.0066, α_s = -1.0°, and 1000 V actuation. Each figure presents the vibratory loads for the blade flapwise bending moment at 0.29R, the blade torsional moment at 0.34R, and the pitch link load for actuation frequencies of 3P (figure 21), 4P (figure 22), and 5P (figure 23). Dashed lines and solid circles present the CAMRAD II results, and solid lines and

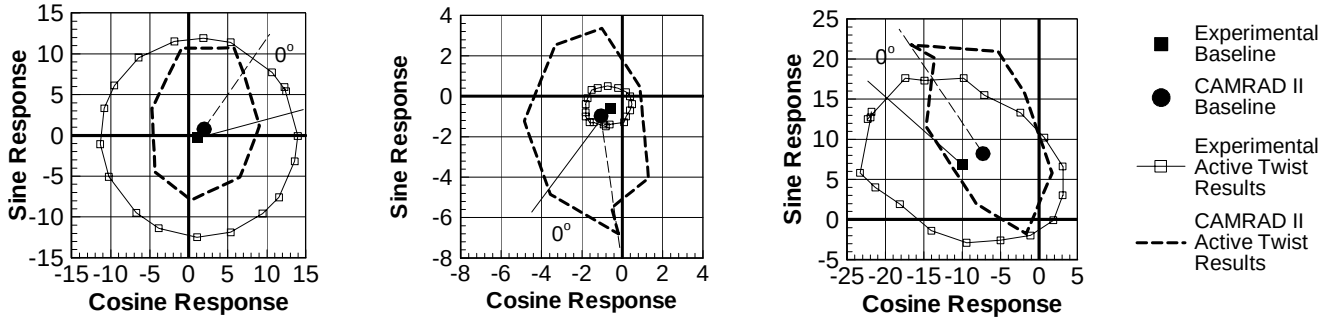

(a) 3P blade torsion moment (r/R = 0.34), in-lb (b) 3P pitch link load, lb (c) 3P blade flapwise moment (r/R = 0.29), in-lb

Figure 21. Comparison of CAMRAD II and experimental 3P rotating-system response to 3P, 1000 V IBC actuation. μ = 0.140, C_L = 0.0066, α_s = -1.0°.

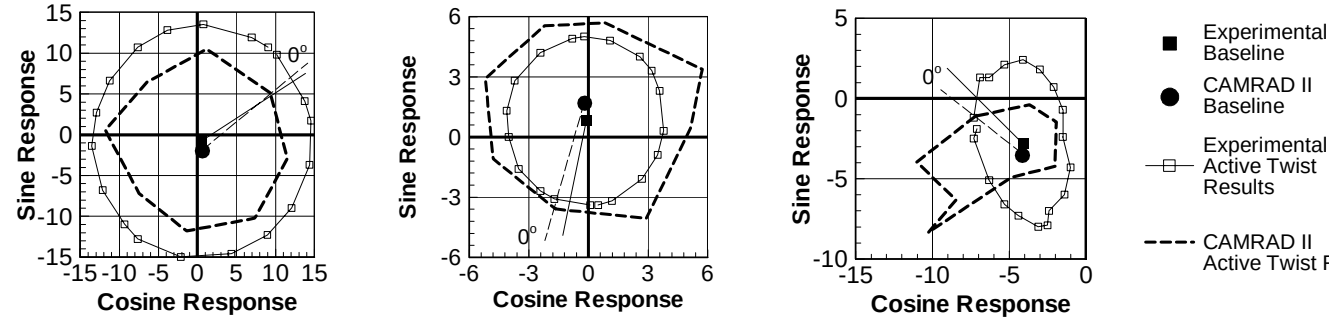

(a) 4P blade torsion moment (r/R = 0.34), in-lb (b) 4P pitch link load, lb (c) 4P blade flapwise moment (r/R = 0.29), in-lb

Figure 22. Comparison of CAMRAD II and experimental 4P rotating-system response to 4P, 1000 V IBC actuation. μ = 0.140, C_L = 0.0066, α_s = -1.0°.

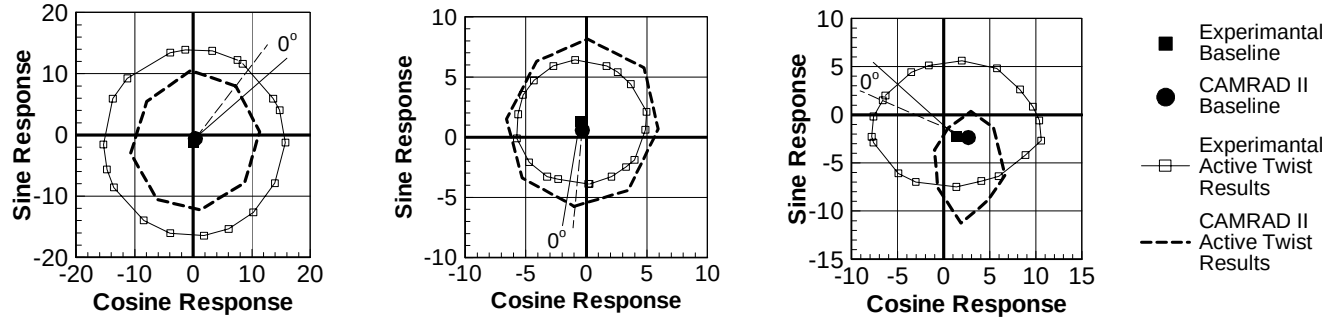

(a) 5P blade torsion moment (r/R = 0.34), in-lb (b) 5P pitch link load, lb (c) 5P blade flapwise moment (r/R = 0.29), in-lb

Figure 23. Comparison of CAMRAD II and experimental 5P rotating-system response to 5P, 1000 V IBC actuation. μ = 0.140, C_L = 0.0066, α_s = -1.0°.

open squares the experimental results. For simplicity, comparisons are shown only for the response results corresponding to the actuation frequency (e.g., 3P response due to 3P actuation). Overall, the baseline rotor response (solid circles and squares) is predicted well by the CAMRAD II model. When the blades are actuated, the analysis generally under-predicts the magnitude of the blade torsional moment response (figures 21a, 22a, and 23a). As the actuation frequency increases, the shape of the CAMRAD II torsional response becomes more circular, matching the experimental results more closely. Likewise, at higher actuation frequencies the relative location of the 0° control phase case is predicted more accurately. Similar trends are observed in the pitch link forces (figures 21b, 22b, and 23b), except that CAMRAD II generally over-predicts the pitch link load magnitude due to actuation, especially for the 3P actuation case.

The CAMRAD II results for the blade flapwise bending moment response (figures 21c, 22c, and 23c) are not as good as those calculated for the blade torsion moment or the pitch link load. However, the relative location of the 0° control phase case is accurately predicted for all three actuation frequencies.

The worst comparisons are for the blade chordwise bending moments (not presented), in which CAMRAD II consistently over-predicts the magnitude of response for all three actuation frequencies and does not accurately predict the relative location of the 0° control phase case.

The analysis-to-experimental comparisons presented in figures 21 through 23 are encouraging in that the general trends of the response to active twist amplitude and control phase are captured reasonably well. While this initial study is not intended to be an exhaustive comparison, it lays the groundwork for the development of more sophisticated models of the Active Twist Rotor system in the CAMRAD II analysis package and provides some confidence that CAMRAD II is applicable to active twist design studies.

Conclusions

Further examination of the vibratory loads reduction results from the initial forward flight test of the NASA/Army/MIT Active Twist Rotor in the Langley Transonic Dynamics Tunnel has been conducted. The active blade twist concept continues to show significant promise for rotorcraft vibration reduction applications utilizing piezoelectric actuators.

Based on the results presented in this paper the following conclusions have been reached:

1. Both rotating- and fixed-system vibratory loads can be dramatically affected using active blade twist control. Using IBC twist control, reductions in vibratory loading of up to 100% are evident for the blade bending moments, pitch link load, and all fixed-system loads other than yawing moment. Maximum reductions in vibratory loading are dependent upon flight condition, active twist control voltage amplitude, and control phase. For all conditions tested, the magnitude of blade torsion moment response was significantly higher for active-twist control than for the baseline, no control, conditions.

2. The size of the vibration reduction control authority region is generally unaffected by changes in rotor shaft pitch, however, the region of control authority grows larger as forward flight speed increases. The capacity for active-twist control to eliminate a specific load is dependent upon the location of the baseline (no control) response in the response map and the overall size of the control authority region.

3. The power necessary to operate the four Active Twist Rotor blades is, at most, less than 0.9% of the maximum rotor power required during testing.

4. The limited CAMRAD II analysis results presented offer reasonably good comparisons with the low-speed flight results from the test. The blade torsion and pitch link load comparisons are the best, while the blade flapwise bending moment comparisons are generally acceptable. For most cases presented, the baseline response is predicted well. Comparison of the response due to active twist varies somewhat, however, the relative position of the 0° control phase case is generally well predicted, providing some confidence that CAMRAD II is useful for active twist design and analysis.

References

1. Loewy, R., “Recent Developments in Smart Structures with Aeronautical Applications,” Smart Materials and Structures, Vol. 6, 1997, pp. 11-42.

2. Samak, D. and Chopra, I., “A Feasibility Study to Build a Smart Rotor: Trailing Edge Flap Actuation,” SPIE Smart Structures and Materials Conference, Vol. 1917, Part 1, 1993, pp. 225-237.

3. Straub, F., “A Feasibility Study of Using Smart Materials for Rotor Control,” American Helicopter Society 49th Annual Forum Proceedings, St. Louis, MO, May 1993.

4. Millott, T. and Friedmann, P., “Vibration Reduction in Helicopter Rotors Using an Actively Controlled Partial Span Trailing Edge Flap Located on the Blade,” NASA Contractor Report 4611, June 1994.

5. Fulton, M and Ormiston, R., “Hover Testing of a Small-Scale Rotor with On-Blade Elevons,” American Helicopter Society 53rd Annual Forum Proceedings, Virginia Beach, VA, April 29 - May 1, 1997.

6. Fulton, M., “Design of the Active Elevon Rotor for Low Vibration,” American Helicopter Society Aeromechanics Specialists Meeting, Atlanta, GA, November 2000.

7. Koratkar, N. and Chopra, I., “Wind Tunnel Testing of a Mach-Scaled Rotor Model with Trailing-Edge Flaps,” American Helicopter Society 56th Annual Forum Proceedings, Virginia Beach, VA, May 2000.

8. Derham, R., Weems, D., Mathew, M., and Bussom, R., “The Design Evolution of an Active Materials Rotor,” American Helicopter Society 57th Annual Forum Proceedings, Washington, DC, May 2001.

9. Barret, R., “Intelligent Rotor Blade Structures Development Using Directionally Attached Piezoelectric Crystals,” M.S. thesis, University of Maryland, College Park, MD, 1990.

10. Chen, P.C. and Chopra, I., “Wind Tunnel Testing of a Smart Rotor with Induced Strain Actuation of Blade Twist.” AIAA Journal, Vol. 35(1), pp. 6-16, 1997.

11. Rodgers, J. P., and Hagood, N. W., “Development of an Integral Twist-Actuated Rotor Blade for Individual Blade Control,” Active Materials and Structures Laboratory, AMSL Report #98-6, Massachusetts Institute of Technology, October 1998.

12. Wilkie, W. K., Wilbur, M. L., Mirick, P. H., Cesnik, C. E. S., and Shin, S. J., “Aeroelastic Analysis of the NASA/Army/MIT Active Twist Rotor,” American Helicopter Society 55th Annual Forum Proceedings, Montreal, Canada, May 25-27, 1999.

13. Cesnik, C. E. S., Shin, S. J., Wilkie, W. K., Wilbur, M. L., and Mirick, P. H., “Modeling, Design, and Testing of the NASA/Army/MIT Active Twist Rotor Prototype Blade,” American Helicopter Society 55th Annual Forum Proceedings, Montreal, Canada, May 1999.

14. Shin, SangJoon, and Cesnik, Carlos E. S., “Design, Manufacturing and Testing of an Active Twist Rotor,” Active Materials and Structures Laboratory, AMSL Report #99-3, Massachusetts Institute of Technology, June 1999.

15. Wilbur, M. L., Yeager, W.T., Jr., Wilkie, W. K., Cesnik, C. E. S., and Shin, S. J., “Hover Testing of the NASA/Army/MIT Active Twist Rotor Prototype Blade,” American Helicopter Society 56th Annual Forum Proceedings, Virginia Beach, VA, May 2000.

16. Wilbur, M. L., Mirick, P. H., Yeager, W. T., Jr., Langston, C. W., Cesnik, C. E. S., Shin, S. J., “Vibratory Loads Reduction Testing of the NASA/Army/MIT Active Twist Rotor,” American Helicopter Society 57th Annual Forum Proceedings, Washington, D. C., May 2001.

17. Wilkie, W. K., et. al., “Low-Cost Piezocomposite Actuator for Structural Control Applications,” SPIE 7th Annual International Symposium on Smart Structures and Materials, Newport Beach, CA, March 2000.

18. Yeager, W. T., Jr., Mirick, P. H., Hamouda, M-N., Wilbur, M. L., Singleton, J. D., and Wilkie, W. K., “Rotorcraft Aeroelastic Testing in the Langley Transonic Dynamics Tunnel,” Journal of the American Helicopter Society, Vol. 38, No. 3, July 1993, pp. 73-82.

19. Booth, E. R. and Wilbur, M. L., “Acoustic Aspects of Active Twist Rotor Control,” American Helicopter Society 58th Annual Forum Proceedings, Montreal, Canada, June 2002.

20. Johnson, W., CAMRAD II, Comprehensive Anaytical Model of Rotorcraft Aerodynamics and Dynamics, Johnson Aeronautics, Palo Alto, California, 1994.